Evaluation of a Mouse-Sized Radial Gradiometer Receive Coil for Magnetic Particle Imaging

Franziska Schrank, Harald Radermacher, Jochen Franke, Sébastien Breham, Fabian Kiessling, and Volkmar Schulz, *Senior Member, IEEE*

***Abstract*—Magnetic particle imaging (MPI) uses the nonlinear magnetization response of superparamagnetic iron-oxide nanoparticles (SPIONs) for fast, sensitive, and quantitative imaging of SPION distributions in biological systems. However, the SPIONs' signal is overshadowed by the much larger excitation signal, necessitating the use of gradiometric receive coils, which often suffer from reduced homogeneity and adverse crosstalk with the MPI system. We develop a new high-sensitivity receive coil by extending the radial geometric design for gradiometers, where cancellation coil parts have a larger diameter, thus providing stronger coupling to the excitation field. This enables us to both reduce cancellation coil windings and increase the winding density of the smaller diameter pickup coil part, achieving greater sensitivity and homogeneity. The developed mouse-sized receive-only (Rx) coil is optimized for the use in Bruker's preclinical MPI scanner, and its performance is compared to the scanner's built-in transmit-receive (TxRx) coil. Power transfer measurements and the particle signal-to-noise ratio (SNR) show a sensitivity improvement of (20–21) dB in the range of (10^2–10^3) kHz compared to the TxRx coil. The sensitivity varies within ±9% across the field of view (FOV), providing higher homogeneity than standard gradiometers. With reconstructed images of SPION dilutions using perimag (Registered trademark) particles, we show an iron limit of detection (LOD) of 8.5 ng for the novel Rx coil, which is a tenfold improvement compared to the original TxRx coil. The high sensitivity and homogeneity provided by the Rx coil will advance the application of MPI in preclinical research by enabling the visualization and quantification of lower iron concentrations, as well as providing higher spatial and temporal resolutions.**

***Index Terms*—Gradiometer, iron detection sensitivity, magnetic particle imaging (MPI), superparamagnetic iron-oxide nanoparticles (SPIONs).**

I. INTRODUCTION

MAGNETIC particle imaging (MPI) is a tracer-based medical imaging technology, first introduced by Gleich and Weizenecker [1]. It leverages the magnetization response of superparamagnetic iron-oxide nanoparticles (SPIONs) to external magnetic fields, thus enabling fast, quantitative, and noninvasive imaging of SPION distributions in biological systems. MPI shows promising applications in fields such as vascular and perfusion imaging [2], [3], [4], [5], oncology imaging [6], [7], [8], and cell tracking [9], [10], [11], [12], [13]. While all these applications benefit from MPI's high specificity for SPION detection, pushing the limits in sensitivity will allow the visualization of lower iron quantities and provide improvements in spatial and temporal resolutions.

The sensitivity in MPI is influenced by many factors, including the type of SPIONs, the scanner geometry, imaging parameters, and the reconstruction scheme. In this work, we focus on the MPI scanner, specifically the receive coil. As with magnetic resonance imaging, local receive coils are a versatile way of increasing the sensitivity of the MPI system for special applications. However, in contrast to magnetic resonance imaging, the particle signal is detected simultaneously during excitation, leading to a massive feedthrough of the excitation signal into the receive coil.

A common technique to eliminate this feedthrough signal is by using notch filters in the receive path that explicitly suppress the frequency of the excitation signal, while the higher harmonic particle signal can pass. However, this also eliminates the strongest particle signal component at the fundamental harmonic. Moreover, in real systems, a nonlinear behavior of hardware components leads to the generation of higher harmonics in the excitation signal that passes the notch filter. This heavily decreases the overall signal-to-noise ratio (SNR) and, consequently, the sensitivity of the scanner.

To reduce the excitation feedthrough across a wide frequency range, gradiometric receive coils have been proposed [14], [15], [16]. These coils attempt to minimize the inductive coupling between the exciting and receiving coils (field orthogonality) over a wide bandwidth. They consist of a pickup coil section, and one or more canceling coil sections wound in opposite directions.

The gradiometric design is very versatile and has been used for different MPI systems, including small-bore field-free point (FFP) MPI [17], [18], [19], [20], traveling-wave MPI [4], [21], field-free line and single-sided MPI [22], [23], [24], [25], and

Received 5 February 2025; revised 7 April 2025; accepted 19 April 2025. Date of publication 12 May 2025; date of current version 5 June 2025. This work was supported by the Deutsche Forschungsgemeinschaft (DFG, German Research Foundation) under Project 441892463 and Project 403039938. The Associate Editor coordinating the review process was Dr. Maryam Shamgholi. *(Corresponding author: Franziska Schrank.)*

Franziska Schrank and Harald Radermacher are with the Institute of Imaging and Computer Vision and the Institute for Experimental Molecular Imaging, RWTH Aachen University, 52062 Aachen, Germany (e-mail: franziska.schrank@lfb.rwth-aachen.de).

Jochen Franke is with Bruker BioSpin GmbH and Co. KG, 76275 Ettlingen, Germany.

Sébastien Breham is with Bruker France SAS, 67166 Wissembourg, France.

Fabian Kiessling is with the Institute for Experimental Molecular Imaging, RWTH Aachen University, 52062 Aachen, Germany.

Volkmar Schulz is with the Institute of Imaging and Computer Vision and the Institute for Experimental Molecular Imaging, RWTH Aachen University, 52062 Aachen, Germany, and also with the Fraunhofer Institute for Digital Medicine MEVIS, 52074 Aachen, Germany.

Digital Object Identifier 10.1109/TIM.2025.3568947

even human head-sized MPI systems [26], [27]. Since the physical principles of signal generation and acquisition are the same for all MPI systems, we can focus on preclinical FFP MPI using Bruker's (Bruker BioSpin GmbH and Co. KG, Ettlingen, Germany) preclinical MPI scanner while the presented concepts can also be translated to other systems.

Bruker's MPI scanner originally features a dual-purpose coil that simultaneously transmits and receives signals. The feedthrough at the excitation frequency is suppressed using a voltage divider and a notch filter, letting higher harmonics of the excitation signal pass. Graeser et al. [17] propose a dedicated receive-only (Rx) coil for this scanner featuring the most common gradiometric setup, which includes a pickup coil part flanked with two cancellation coil parts of the same radius. However, this setup essentially creates "zeros" at the transition from pickup to cancellation coil part, and the sensitivity profile inside the pickup coil part declines steeply. Paysen et al. [18] present a radial geometry of the gradiometric receive coil, in which the cancellation coil parts have a larger diameter than the pickup coil part, thus eliminating the zeros and achieving an overall higher homogeneity. However, Paysen et al. [18] do not exploit the full potential of this approach, which is used to explicitly leverage the uneven coupling of the coil parts with the excitation field due to their differing diameters. Increasing the cancellation coil diameter enables the use of fewer coil windings for the feedthrough cancellation. Both fewer coil windings and the increased distance to the particle specimen decrease the unwanted detection and thus cancellation of the particle signal in the cancellation coil parts. At the same time, the coil windings in the pickup coil part can be increased to maximize particle signal detection. Furthermore, Paysen et al. [18] place the cancellation coil parts on top of the pickup coil parts, which increases the homogeneity but significantly attenuates the particle signal that is induced in both pickup and cancellation coil parts.

We propose a novel radial gradiometric receive coil that features two cancellation coil parts, axially positioned outside one pickup coil part. The cancellation coil parts have a larger diameter and fewer windings, and the pickup coil part has a smaller diameter and higher winding density than the one presented by Paysen et al. [18], to fully leverage the potential of the radial geometric design for increased sensitivity and homogeneity. This novel coil was jointly designed with and built by Bruker to fit their commercial Preclinical MPI 25/20 FF scanner. The inductance and capacitance of the receive coil have also been optimized to ensure compatibility with a dedicated low-noise amplifier from Bruker and to minimize overlap with the MPI system. Thus, the receive path's inherent noise is reduced overall. In general, gradiometric receive coils have to be positioned very precisely inside the excitation field for optimal feedthrough cancellation, as well as to prevent skewed sensitivity profiles, as can be observed in [17]. Thus, the new receive coil includes a mechanical scaffold and fixation mechanisms ensuring precise and reproducible positioning.

The purpose of this article is to provide a comprehensive characterization of the new receive coil, in direct comparison to the original MPI system. We follow the procedure established by Paysen et al. [18] and perform simulations of the coil's sensitivity, measure it with a network analyzer (NA), and analyze the system's background signal and particle SNR. Furthermore, phantoms with decreasing iron concentrations are measured and reconstructed to perform an image-based analysis of the system's iron limit of detection (LOD). Finally, the achievable spatial resolution is analyzed with a phantom experiment. For the particle measurements, we use perimag[1] (micromod Partikeltechnologie GmbH, Rostock, Germany; [28]), to show the outstanding capabilities of our novel coil design with a commercially available tracer.

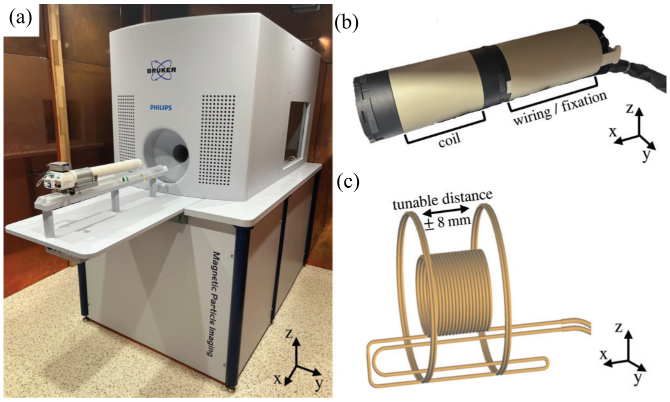

Fig. 1. (a) MPI scanner (Preclinical MPI 25/20 FF, Bruker BioSpin GmbH and Co. KG), installed in a shielded room. (b) Photograph of the Rx coil with the actual coil (left) and the connecting wires and fixation (right). (c) Drawing of the coil with the inner pickup coil part and the outer cancellation coil parts wound in opposing winding direction.

II. Materials and Methods

In the following, the used MPI system and the newly developed dedicated receive coil will be introduced. Additionally, the performed simulations and measurements evaluating the sensitivity of the system with and without the receive coil are described. For all measurements that are performed with the original system, the new receive coil is completely removed from the scanner bore to ensure unrestricted operation.

A. MPI System Hardware

The used MPI system is the Preclinical MPI 25/20 FF (Bruker BioSpin GmbH and Co. KG) installed at RWTH Aachen University [Fig. 1(a)]. In this system, spatial encoding of the SPIONs' magnetization response is achieved using an FFP, created by two electromagnets with opposing polarities. The FFP is moved through space by superimposing three orthogonal drive fields (DFs) that create homogeneous sinusoidal magnetic fields at similar frequencies. These frequencies are 2.5 MHz/(102,96,99) in x-, y-, and z-directions, respectively, resulting in a closed Lissajous trajectory. This trajectory is scanned with a repetition time of approximately 21.5 ms, or 46 times/s. The DF field of view (FOV), meaning the extension of the scanned volume, is given by the ratio between DF amplitude and gradient field strength. The maximum DF amplitude that can be set is 14 mT/μ_0 in all directions and

---

[1] Registered trademark.

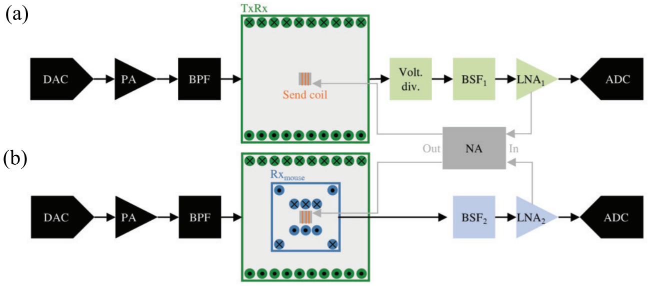

Fig. 2. (a) Scheme of the TxRx chain for TxRx and (b) Rx$_{\text{mouse}}$ coil. The excitation signal is controlled by a DAC, followed by a PA to amplify the currents and a BPF tuned to the channel frequency before entering the excitation coil. The receive signal from the TxRx coil passes a voltage divider, is filtered with a BSF set to the excitation frequency, and amplified by an LNA before entering an ADC. For the Rx$_{\text{mouse}}$ coil's signal, no voltage divider is needed, and a different BSF and LNA are used. For initial sensitivity measurements, an NA is used, connected to the LNA and a small send coil inside the scanner.

the maximum gradient field strength of the selection field coils is 2.5 $\text{T/m}/\mu_0$ in the strongest direction (z-direction) and 1.25 $\text{T/m}/\mu_0$ in x- and y-directions, where the x-axis is parallel to the scanner bore. This results in a DF FOV of $(22.4 \times 22.4 \times 11.2)\text{mm}^3$. For image reconstruction, the system-matrix-based approach is used [29].

B. MPI Receive Coil Hardware

The original x-axis receive coil is a combined transmit-receive (TxRx) coil, consisting of a solenoid with a diameter of 160 mm made of 25 turns of high-frequency (HF) Litz wire. The excitation signal is controlled by a digital-to-analog converter (DAC) and then passes a power amplifier (PA) and a bandpass filter (BPF), tuned to the excitation frequency, before entering the resonant circuit with the TxRx coil. A frequency-dependent voltage divider is used to feed the higher harmonic components present in the TxRx coil's signal to the following band-stop filter (BSF) and low noise amplifier (LNA). Due to this direct connection between the transmit and receive paths of the system, the receive signal is at high risk for distortions, such as higher harmonics of the excitation signal arising from a nonlinear behavior of the connected hardware components. Schematically, the receive path is illustrated in Fig. 2(a).

The dedicated Rx coil, subject to this article, is designed as a radial gradiometer [Fig. 1(b) and (c)], i.e., the cancellation coil parts are placed radially outward at a larger diameter than the pickup coil part [18]. In order to have a high geometric gain, the pickup coil windings are placed as close to the FOV as possible. For a mouse-sized FOV, this results in an inner coil diameter of 48 mm (1 × 18 turns of copper HF Litz wire). The diameter of the two cancellation coil parts placed next to the pickup coil part is maximized, resulting in inner diameters of 105 mm (1 × 2 turns of HF Litz wire each). The number of turns in the cancellation coil parts was deliberately minimized to reduce the coupling of particle signal into these, while a high coupling to the excitation field is given by the large covered area. The number of layers and the wire diameter were chosen based on the simulations for optimal matching to the dedicated LNA, resulting in a wire diameter of 2.4 mm, consisting of 600×71 μm diameter filaments. This comparatively thick Litz wire, as well as using a twisted connection cable, also minimizes the impedance of the coil. The LNA has a noise value of 71 $\text{pV}/\sqrt{\text{Hz}}$ at 100 kHz and amplifies the signal by +44 dB. The cancellation coil parts can be shifted symmetrically along the x-axis by ±8 mm to minimize the mutual inductance with the excitation field, which, in turn, minimizes the coupling of distortions, which are present in the transmit path, into the receive path. The overall wiring was also optimized to minimize the mutual inductance to the y- and z-channels of the MPI system. In contrast to the original TxRx coil, the Rx coil does not need a voltage divider and is, thus, directly connected to the BSF, which minimizes additional losses in the receive chain [see Fig. 2(b)]. Built into the mechanical scaffold [Fig. 1(b)], the coil can be easily integrated into the system by sliding it into the scanner bore and fixing it axially with a metal pin and radially with a clamping mechanism, allowing firm and reproducible concentric placement. The mechanical structure of the coil is mainly manufactured by selective laser sintering (SLS) from synthetic powder. No magnetic materials are used throughout the coil design, and only the coil itself and a Pt100 sensor, which is integrated into the coil for temperature surveillance, are conductive.

The Rx coil reduces the scanner's accessible bore diameter from originally 120 to 45 mm, allowing the imaging of phantoms or mice. Thus, in the following, we will refer to our Rx coil as Rx$_{\text{mouse}}$ coil, in contrast to the Rx$_{\text{rat}}$ coil capable of imaging rats presented by Paysen et al. [18]. According to an estimation for the sensitivity ρ in the center of an LNA-noise dominated solenoid coil with radius R [17], the sensitivity of the Rx$_{\text{mouse}}$ coil is expected to be increased by 16 dB compared to the built-in TxRx coil.

C. Sensitivity Profile Simulation and Measurement

The first measurement to investigate the sensitivity is a measurement of the power transfer using an NA (Keysight E5061B ENA, Santa Rosa, CA, USA). The NA is placed outside the MPI room and connected to a small send coil positioned in the center of the MPI bore using a ~10-m-long cable. This cable is included in the power transfer baseline calibration of the NA. The send coil, made of enameled copper wire wound three times around a 3-D-printed cubic carrier (edge length of 7 mm), generates a reference signal in the x-direction. The output of either the TxRx or the Rx$_{\text{mouse}}$ coil's LNA is connected to the input of the NA (see Fig. 2). The power transfer is investigated with a frequency sweep from 10 kHz to 2 MHz, which includes the receive bandwidth of the scanner of 1.25 MHz. With the excitation at 25 kHz, this frequency range covers up to the 50th harmonic, which is highly sufficient for MPI applications. Furthermore, higher excitation frequencies are uncommon in MPI, due to physiological limits in magnetostimulation and specific absorption rate (SAR) [30]. To evaluate the spatial sensitivity profiles of the coils, the send coil is also moved to different positions on the x- and y-axes. All NA measurements are averaged 64 times. This power transfer measurement is an established procedure to compare receive chains in MPI [18], [31] and can also be used to transfer the device-specific receive signal into a device-independent domain. We refer interested readers to the study on receive path calibration by Thieben et al. [32].

The measured spatial sensitivity profiles are then compared to simulations of the magnetic fields created by the coils at unit current, carried out in MFS5 (Würzburg; [33]). By law of reciprocity, the magnetic field distribution of a coil is equivalent to its spatial sensitivity. However, ideal stand-alone coils are assumed, neglecting mutual inductances and eddy current effects in adjacent structures as well as within the coils. Thus, only the relative deviations of the magnetic fields in comparison to the center of the coils are investigated.

D. System Matrix Acquisition

To perform image reconstruction with the MPI system, a system matrix has to be acquired in a calibration scan. For all particle measurements, including the system matrix, plain perimag is used, as it is a commercially available MPI-tailored tracer that is widely used in the MPI community for applications such as real-time flow measurements [4], [34], [35], cell tracking [9], [36], and temperature and viscosity estimation [37], [38], [39], [40], [41]. The used particle sample contains 1 μL of perimag (stock iron concentration is 8.5 mg/mL), filled into a cubic-shaped 1-mm^3 sample tube (Bruker BioSpin GmbH and Co. KG). The MPI scanner is set to 12-mT DF amplitude, as in [18]. This DF amplitude leads to a DF FOV, meaning the extension of the closed Lissajous trajectory, of $(19.2 \times 19.2 \times 9.6)$ mm^3. As shown in [42], the best reconstruction results are achieved with system matrices that extend beyond the DF FOV. Thus, the system matrices are acquired on a grid of $(23 \times 23 \times 13)$ voxels, covering an FOV of $(23 \times 23 \times 13)$ mm^3. This is also the largest FOV that can be sampled in the Rx_{mouse} coil due to the mechanical restriction in bore size. Every 23 positions, empty scanner measurements are performed, which are interpolated and used for background correction to account for eventual background drifts [43]. All measurements are executed with 100 averages, resulting in a total acquisition time of 7 h 12 m and a data size of 8.3 Gbyte for one system matrix. System matrices are acquired separately for TxRx and Rx_{mouse} coils.

E. Serial Dilution Measurement

The iron LOD of both coils is evaluated by measuring particle samples at decreasing iron concentrations. To this end, 15 samples are prepared, each containing 5 μL of perimag water mixture at iron concentrations ranging from c(Fe) = 0.85mg/mL down to c(Fe) = 85 ng/mL (total iron mass ranging from m(Fe) = 4250ng to m(Fe) = 0.4ng). The dilution mixtures are filled into 0.2-mL VWR[1] PCR tubes (VWR International GmbH, Darmstadt, Germany). The volume of 5 μL is chosen to minimize the influence of the MPI encoding scheme on the measurement [17], while also minimizing pipetting and positioning errors. Small amounts of fluid are difficult to position in the sample tubes as the fluid drop tends to stick to the side of the tube, resulting in slight deviations in the positioning in the MPI scanner that influence the measured signal. While this is also a challenge using the 1-μL reference sample tubes for the system matrix measurement, here all individual measurements inside the system matrix would have the same offset in positioning, which would, in turn, influence all reconstruction results equally and is, therefore, negligible.

With the Rx_{mouse} coil, all 15 samples are measured, while only the nine samples with the highest iron contents are measured with the TxRx coil (the lowest m(Fe) = 10.6 ng) as the LOD is expected to be around 100 ng [18]. The samples are measured five times at three different locations in the FOV, namely, $A = (-5, -5, 0)$ mm, $B = (0, 0, 0)$ mm, and $C = (5, 5, 0)$ mm, as suggested by Paysen et al. [18]. Every measurement is averaged 100 times, leading to a measurement time of 2.15 s. The samples are positioned inside the scanner bore with a rod attached to a three-axis robot. To correct all sample measurements for systematic noise caused by the scanner, the robot, the mounting rod, and the PCR tubes, measurements of an empty PCR tube mounted on the rod are performed at the same positions as the sample measurements. These measurements are also repeated five times, and each of them is subtracted from each sample measurement at the same position, resulting in 25 individual corrected measurements for each dilution at each position. The particle samples are compared to a sample containing 5 μL of water, which is measured and processed the same way.

Image reconstruction is performed using the Kaczmarz algorithm with Tikhonov regularization and positivity constraint [44], implemented in Python. Frequency components below 80 kHz are affected by the BSF and thus excluded before reconstruction. Furthermore, frequencies with high SNR are preferred, and based on visual inspection of the reconstructed MPI images, the 150 frequency components with the highest SNR were chosen for both the TxRx and the Rx_{mouse} coil. For the TxRx coil, this includes frequency components down to an SNR of 18 and for the Rx_{mouse} coil down to 95. The regularization is chosen to be $150 \cdot \lambda_0$, with $\lambda_0 = \text{trace}(\mathbf{S}^H \mathbf{S})/\text{N}$, where $\mathbf{S} \in \mathbb{C}^{\text{M} \times \text{N}}$ is the system matrix with M frequency components and N spatial positions and H denotes the Hermitian conjugation [45]. The reconstruction algorithm is run for one iteration, and the parameters are kept the same for all reconstructions of one coil to ensure comparability of the resulting image intensities.

To quantitatively evaluate the reconstructed intensities, the pixel intensities at the sample positions are summed and compared to the iron content of the sample. For this, a region of interest (ROI) of $(6 \times 6 \times 3)$ mm^3 around the known sample position is chosen, and all voxels inside this ROI are summed if their intensity is larger than 25% of the maximum intensity in the ROI. This thresholding is performed to minimize influences from image blurring that is introduced in the regularized reconstruction [18]. Each measurement is reconstructed individually so that the mean and standard deviation can be calculated over the 25 reconstructions for every dilution and every position.

F. Spatial Resolution Measurement

To assess the spatial resolution achievable with the TxRx and the Rx_{mouse} coil, we use a phantom made out of PMMA that features bores with a diameter of 0.5 mm and a depth of

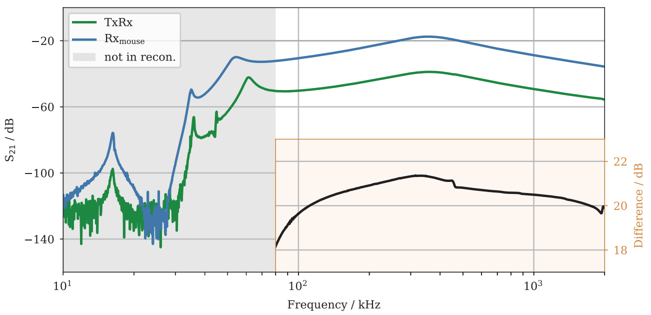

Fig. 3. Power transfer (S_{21}) measured with a send coil positioned in the center of the scanner, connected to the NA output and receive signal of TxRx or $\mathrm{Rx}_{\mathrm{mouse}}$ coil's LNA connected to the NA input. A frequency sweep from 10 kHz to 2 MHz is performed. The inlay shows the difference of $\mathrm{Rx}_{\mathrm{mouse}}$ to TxRx coil signal in the range of 80 kHz–2 MHz. Frequencies below 80 kHz (gray) are not used in reconstruction.

3 mm arranged in a V-shaped pattern. The bores are placed between 2 and 6 mm apart, measured from center to center, which corresponds to distances from 1.5 to 5.5 mm edge-to-edge. More information on the phantom can be found in [31]. The bores were filled with perimag at stock solution (8.5 mg/mL), and the phantom was placed inside the scanner bore using the robot. Image acquisition was performed with the same parameters as for the system matrix and the dilution series. Background measurements of the empty scanner were subtracted from the phantom measurements before reconstruction. For image reconstruction, the parameters were set based on visual inspection of the reconstruction results, resulting in an SNR cutoff of 1.5 and 150 Kaczmarz iterations for both coils but a regularization of $0.1 \cdot \lambda_0$ for TxRx and $0.0005 \cdot \lambda_0$ for $\mathrm{Rx}_{\mathrm{mouse}}$ coil. Finally, the spatial resolution is evaluated using line profiles across the reconstruction results at the position of the two bores with a distance of 4.5 and 2.5 mm (edge-to-edge).

III. RESULTS

A. Coil Sensitivities

At first, the results for the NA measurements with the send coil positioned in the center of the scanner are analyzed and can be found in Fig. 3. Below 80 kHz, the receive signal is mainly influenced by the BSF, leading to a strong attenuation of around 120 dB of the signal around 25 kHz for both coils, to minimize the feedthrough of the excitation signal. Due to this strong distortion of the signal, the signal in this frequency range is not used in image reconstructions. Above 80 kHz, the sensitivity of both coils increases until about 400 kHz. This maximum exists due to a resonance of the LNAs with the receive coils, and thus, its position and amplitude are influenced by the inductance of the coils. During the $\mathrm{Rx}_{\mathrm{mouse}}$ coil's design process, this maximum was used to optimize the wire diameter and the number of layers in the $\mathrm{Rx}_{\mathrm{mouse}}$ coil. The difference plot that can also be found in Fig. 3 shows a sensitivity increase of 20–21 dB of the $\mathrm{Rx}_{\mathrm{mouse}}$ coil compared to the TxRx coil between 10^2 and 10^3 kHz. This matches the theoretical sensitivity improvement based on the smaller coil radius of 16 dB, with additional improvements due to the matching to the LNA and different receive paths that do, for instance, not feature a voltage divider when using the $\mathrm{Rx}_{\mathrm{mouse}}$ coil.

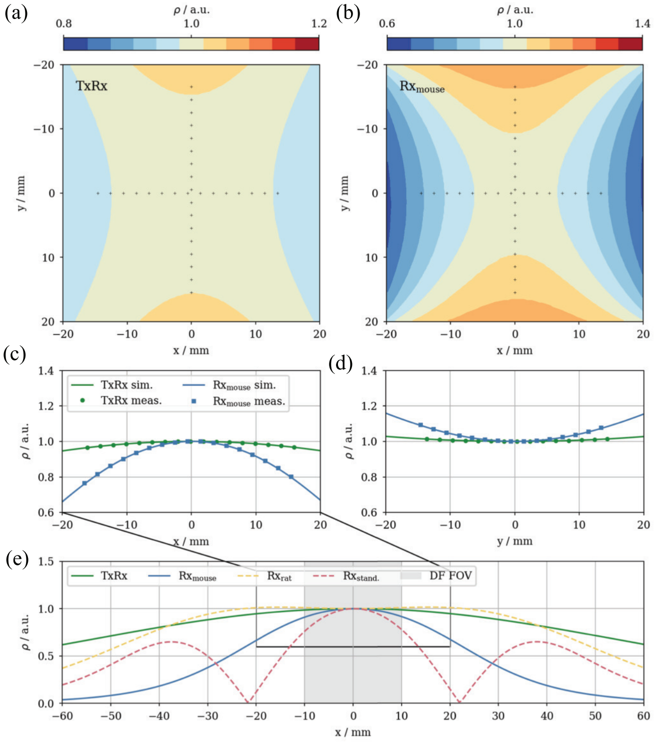

Fig. 4. Simulated sensitivity in central *xy* plane of the (a) TxRx and (b) $\mathrm{Rx}_{\mathrm{mouse}}$ coil. Note different value ranges. The black crosses indicate the send coil measurement positions. Simulated and measured sensitivities for both coils along (c) *x*- and (d) *y*-axes. (e) Simulated sensitivity profile along the *x*-axis for different Rx coils, with coil parameters for $\mathrm{Rx}_{\mathrm{rat}}$ based on [18] and $\mathrm{Rx}_{\mathrm{stand.}}$ based on [17]. In all plots, the central values are set to 1 to compare spatial dependencies.

In Fig. 4(a) and (b), the simulated sensitivities in the central *xy*-plane of the TxRx and the $\mathrm{Rx}_{\mathrm{mouse}}$ coil are shown with the sensitivity in the center of the coils set to 1. Due to rotational symmetry, the behavior in the *y*-direction is the same as in the *z*-direction. Qualitatively, the sensitivity distributions show a similar behavior between TxRx and $\mathrm{Rx}_{\mathrm{mouse}}$ coil although one is a simple solenoid and the other a gradiometer with cancellation coil parts. Note, however, different scaling of the plots. We analyze the homogeneity of the coils in an ROI of $(20 \times 20 \times 10)\ \mathrm{mm}^3$ around the center, which is similar to the DF FOV. For the TxRx coil, this reveals a variation in sensitivity by ±1% relative to the sensitivity in the center, while the sensitivity in the $\mathrm{Rx}_{\mathrm{mouse}}$ coil varies by +5% and −9%. The sensitivity of the $\mathrm{Rx}_{\mathrm{mouse}}$ coil was also simulated for shifts in the cancellation coils ±8 mm along the *x*-axis, achieving deviations from these results below 1%. The plots of the sensitivity planes also show the positions of the send coil in the NA measurements. Both simulated profiles along the *x*- and *y*-axes, as well as extracted maximum amplitudes from the NA measurements, are plotted in Fig. 4(c) and (d). To compare the spatial dependence of the sensitivity between measurement and simulation, the measured values at the center position are also set to 1. Thus, it can be observed that

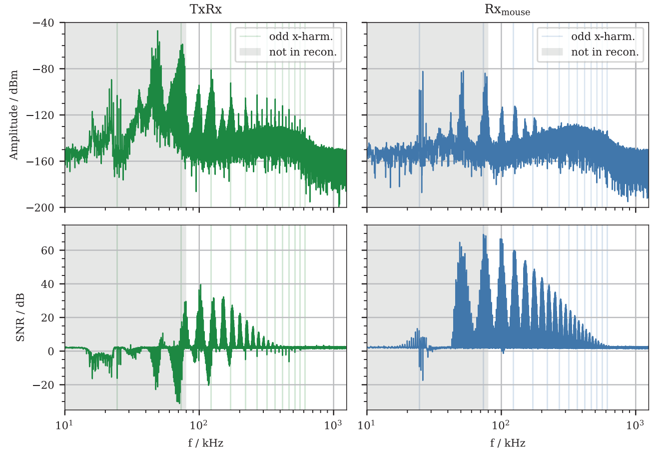

Fig. 5. Raw frequency spectra of empty scanner measurements with TxRx and Rx$_{mouse}$ coil (top). SNR spectra calculated from the system matrix measurements, displayed as root-power quantity in dB (bottom). In all plots, the frequency range until 80 kHz which is not used in reconstruction and odd x-harmonic frequencies between ~25 and ~600 kHz are highlighted.

measurement and simulation follow the same spatial dependence with a relative deviation between simulated and measured values below 1%.

In Fig. 4(e), the simulated sensitivity profiles along the x-axis of the TxRx and the Rx$_{mouse}$ coil are compared to profiles of a radial gradiometer with larger pickup coil radius and to a standard gradiometer with equal pickup and cancellation coil part radius. The simulation of the larger radial gradiometer is based on the Rx$_{rat}$ coil described in [18] and the standard gradiometer on the coil presented in [17], here denoted as Rx$_{stand.}$ coil. The sensitivity profiles are scaled to the sensitivity in the center of the coils. As can be seen, the sensitivity of the Rx$_{stand.}$ coil steeply decreases from the center of the coil toward its zeros, while the Rx$_{mouse}$ coil shows a more shallow slope and no zeros. Both Rx$_{rat}$ and TxRx coil exhibit almost perfect homogeneity across the DF FOV. For the Rx$_{rat}$ coil, this high homogeneity can be attributed to the positioning of the cancellation coil parts on top of the pickup coil parts, which, however, reduces the total sensitivity as the receive signal is partly canceled out. Thus, the Rx$_{mouse}$ coil both maximizes sensitivity and strongly increases homogeneity compared to standard gradiometric approaches.

B. Spectral Analysis and System Matrix

The MPI background signal was measured with the TxRx and the Rx$_{mouse}$ coil, each with 100 measurement averages (2.15-s acquisition time). The acquired signal amplitudes in the frequency domain can be found in Fig. 5. For the TxRx coil, the strongest background signal components are integer multiples of the x-direction excitation frequency, which are caused by nonlinear distortions in the TxRx chain. In the Rx$_{mouse}$ coil background signal, these distortions are highly suppressed due to the broadband decoupling of transmit and receive paths. Thus, the harmonics of the x-excitation are attenuated by up to 56 dB in the Rx$_{mouse}$ coil compared to the TxRx coil. For both coils, signal contributions at mixing terms of all three excitation frequencies can be observed as broad peaks around the excitation frequencies, which is due to the inevitable coupling between orthogonal fields in practice. Above 200 kHz, the background is dominated by the LNA and the analog-to-digital converter (ADC), showing similar behavior and amplitude for TxRx and Rx$_{mouse}$ coil. This noise floor is also present below 200 kHz and neglecting it in both coils results in an attenuation of background signal on average by 10 dB in the Rx$_{mouse}$ coil compared to the TxRx coil.

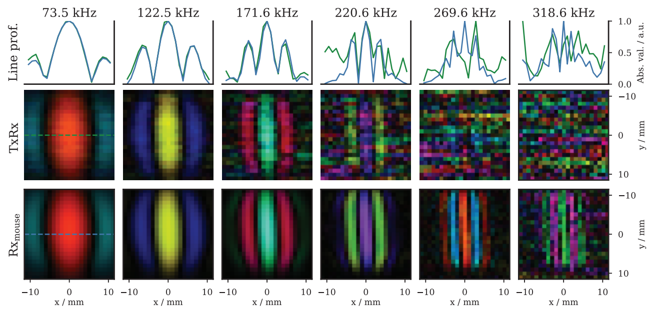

Fig. 6. Comparison of system matrix components measured with TxRx or Rx$_{mouse}$ coil in the central xy-plane. The complex frequencies are RGB-encoded [47]. The selected frequencies are multiples of the x-excitation frequency and are given above the images. The top row shows the normalized absolute values of the frequency components along the x-axis (dotted line in leftmost frequency component).

The system matrices contain a series of particle and background measurements and can thus be used to calculate a particle SNR, which is also shown in Fig. 5. This SNR is calculated for each single measurement by subtracting a corresponding background measurement from the sample measurement and dividing by the standard deviation over all background measurements as a measure of the system noise. Then, all calculated SNR spectra in the system matrix are averaged. As expected, the SNR spectra show high signal around harmonics of the excitation frequencies for both coils [46]. Predominantly, the SNR of the Rx$_{mouse}$ coil is significantly higher than the SNR of the TxRx coil, which even has many frequency components with negative SNR, especially below 200 kHz and at the harmonics of the x-excitation frequency. This leads to an SNR gain of up to 86 dB with the Rx$_{mouse}$ coil. In the frequency range between 100 and 200 kHz, the higher background level in the TxRx coil leads to SNR values around 20–40 dB lower than that of the Rx$_{mouse}$ coil. Between 200 and 300 kHz, there is a nearly constant gain of 20 dB in SNR of Rx$_{mouse}$ coil to TxRx coil, which matches the results of the NA measurements, showing mostly the increase in signal due to the coil's geometry while the noise level in that frequency range is similar in TxRx and Rx$_{mouse}$ coil. Above 300 kHz, the SNR of the TxRx coil vanishes into the noise floor, whereas the SNR of the Rx$_{mouse}$ coil stays above the noise floor until around 600 kHz. Counting the number of frequency components with an SNR >2 results in 1780 components for the TxRx coil and 3920 components for the Rx$_{mouse}$ coil.

Due to the magnetic characteristics of the particle excitation, the system matrix shows spatial dependencies, which vary across frequencies [46]. Some examples of frequency components in the central xy-plane are shown in Fig. 6 for TxRx and Rx$_{mouse}$ coils. The chosen frequencies are harmon-

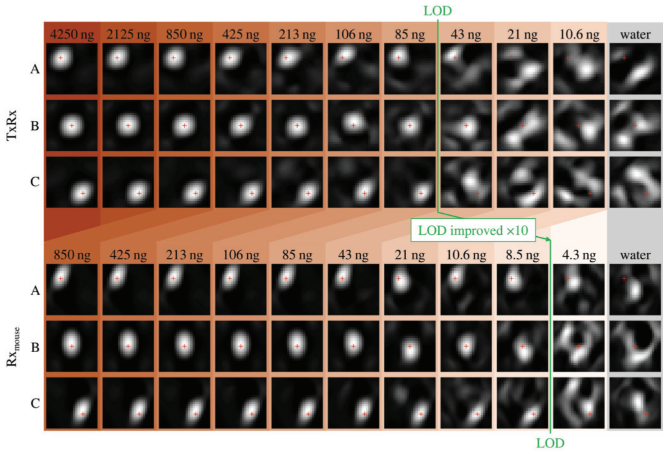

Fig. 7. Reconstructed MPI images of the serial dilution experiment as maximum intensity projections along the z-axis for the TxRx coil (top) and the $\mathrm{Rx}_{\mathrm{mouse}}$ coil (bottom). Above each image, the iron mass of the sample is displayed. Each sample is measured at three locations (A, B, and C) with the actual location marked by a red cross. Each image is scaled to its maximum intensity individually. The LOD is marked in green for each coil.

ics of the x-excitation frequency, showing how the signal decreases for increasing frequencies and vanishes into the noise floor below 300 kHz for the TxRx coil while still being visible for the $\mathrm{Rx}_{\mathrm{mouse}}$ coil. In the top row of Fig. 6, also normalized absolute values of the frequency components along the x-axis are shown to further highlight the similarity between TxRx and $\mathrm{Rx}_{\mathrm{mouse}}$ coils. The slight deviations toward the border of the FOV are consistent with the decrease in sensitivity of the $\mathrm{Rx}_{\mathrm{mouse}}$ coil seen in the spatial NA measurements and simulation (Fig. 4).

C. Serial Dilution Measurements

In Fig. 7, the reconstructed images from the serial dilution experiment can be found. The images show maximum intensity projections along the z-axis, where the brightness is scaled to the maximum of each image individually. The particle samples appear blurred in the images, which is due to both regularization and the frequency component selection, as high-frequency components that are important for spatial resolution and sharpness are neglected due to their low SNR. The lowest iron amount that can be visualized at all three spatial locations is 85 ng for the TxRx coil and 8.5 ng for the $\mathrm{Rx}_{\mathrm{mouse}}$ coil, which is an improvement of a factor 10. These values are selected as the visually identified LOD. Samples with lower amounts of iron cannot be properly located, as the images contain a high amount of noise and artifacts.

As MPI is a quantitative imaging modality, the ability to correlate iron mass with image intensity is tested. In Fig. 8, the extracted intensity values from the images are plotted against the iron mass. Here, the mean over the 25 individual reconstruction results at every location is shown with the standard deviations as the error bars. Both coils show a linear dependence of the MPI signal with the iron content above the visually identified LODs. Linear regressions are performed with all data points above the LODs, and the corresponding coefficients of determination (R^2) are calculated, providing values of $R^2 > 0.98$ for both coils and all three positions, validating the visually identified LODs.

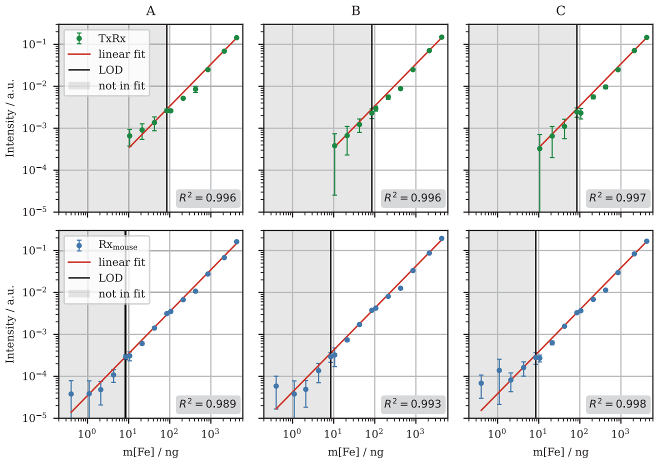

Fig. 8. Reconstructed MPI intensities plotted against the iron mass for TxRx coil (top) and $\mathrm{Rx}_{\mathrm{mouse}}$ coil (bottom). Shown are mean values and standard deviations as error bars over the 25 individual reconstructions for all samples at all positions (A, B, and C). Linear regressions (red lines) were performed with all values above the visually identified LODs (black lines) with coefficients of determination $R^2 > 0.98$ for both coils and all positions.

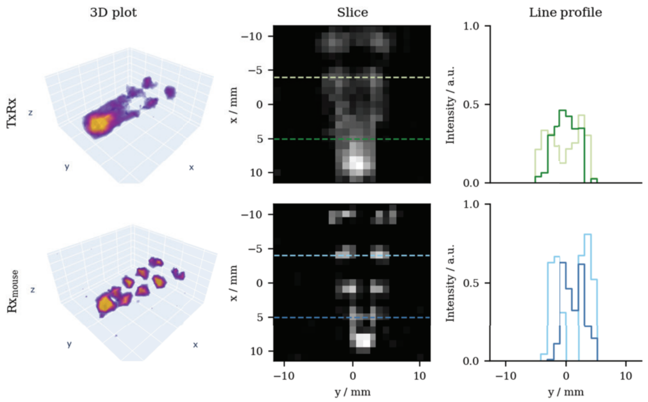

Fig. 9. Reconstruction result of the spatial resolution measurement for the TxRx (top) and the $\mathrm{Rx}_{\mathrm{mouse}}$ coil (bottom). The 3-D visualization of the reconstruction result, slice along $z = 0$, line profiles along the indicated lines (from left to right). The slice images and line profiles are scaled to the maximum intensity in the slices.

D. Spatial Resolution Measurement

In Fig. 9, the results of the spatial resolution measurement with the V phantom can be found. While it is barely possible to recognize the V in the reconstruction result with the TxRx coil, it is clearly visible using the $\mathrm{Rx}_{\mathrm{mouse}}$ coil. To quantify, for the TxRx coil, the bores with the second-largest distance of 4.5 mm (edge-to-edge) can be separated along the line profile but already strongly blur together with the bores below. Thus, the spatial resolution lies between 5.5 and 4.5 mm. For the $\mathrm{Rx}_{\mathrm{mouse}}$ coil, the bores with 2.5 mm distance can be separated along the line profile; however, they also blur with the bores below and the spatial resolution lies between 3.5 and 2.5 mm.

IV. DISCUSSION

A. Comparison to State of the Art

The results of the evaluation of the dedicated $\mathrm{Rx}_{\mathrm{mouse}}$ coil for the Bruker preclinical MPI scanner are summarized in Table I. For comparison, Table I also includes values for the

TABLE I

Overview of Sensitivity Improvement of Rx_{mouse} Compared to TxRx Coil and Rx_{rat} to TxRx Coil as Presented in [18]. The Last Row Shows the Total Iron LOD Achieved by the Two Rx Coils and the Improvement Between These Totals

	Rx_{mouse}	Rx_{rat}	$\text{Rx}_{\text{mouse}}/\text{Rx}_{\text{rat}}$
Theory ($\rho \propto 1/\sqrt{R^3}$)	16 dB	10 dB	6 dB
NA S_{21} [(10^2 – 10^3) kHz]	(20 – 21) dB	12 dB	(8 – 9) dB
SNR [(200 – 300) kHz]	20 dB	10 dB	10 dB
Iron LOD	×10	×6.7	×1.5
Iron LOD (total)	8.5 ng	20 ng	×2.4

Rx_{rat} coil as presented in [18]. Due to the smaller coil radius, the Rx_{mouse} coil had an expected sensitivity improvement of 16 dB and achieved ≥20-dB improvement throughout the NA measurements and the spectral analysis across the MPI relevant frequency range from 10^2 to 10^3 kHz. It is reasonable to assume that the additional 4 dB could come from the LNA and the matching of the Rx_{mouse} coil to it. The Rx_{rat} coil only gained ≤2 dB from theory to measurement, which could be due to the signal attenuation in the cancellation coil parts placed on top of the pickup coil part.

In terms of the measured iron LOD, Paysen et al. [18] achieved 133 ng with the original Bruker MPI system—the TxRx coil—in contrast to the 85 ng presented here. However, they did not test iron contents between 133 and 78 ng; thus, their LOD could also be slightly lower. Another reason for the discrepancy is the used particle type, which is Ferucarbotran (Meito Sangyo, Japan) in their study and perimag in ours. Ferucarbotran is the precursor of Resovist, which was shown to exhibit up to two times lower signal amplitude than perimag at low harmonics and up to 2.5 times lower amplitude for high harmonics [28], [48], [49]. A lower signal amplitude at the same iron content results in a higher iron LOD with these particles. Thus, a lower LOD with perimag is expected. Lastly, although the same MPI system was used, there are slight differences in the built-in electronics, especially in the LNA, as can be seen, for example, in the receive path presented in the NA measurements. Nevertheless, we improve the iron LOD of 20 ng achieved with the Rx_{rat} coil [18] by a factor 2.4 to the LOD of 8.5 ng with the Rx_{mouse} coil. Graeser et al. [17] also use a similar scanner and add a standard gradiometer receive coil with a radius of 20 mm. They use a lower gradient strength of (2,1,1) T/m/μ_0 and different particles, namely, LS-008, and report an LOD of 5 ng. Calculating back with the geometric sensitivity scaling, the Rx_{mouse} coil with a radius of 24 mm has an expected LOD of 6.6 ng. However, the used particles, LS-008, provide three-times higher signal than Ferucarbotran [50], which is even more than the signal gain from perimag over Ferucarbotran of 2. Thus, lower signal and higher LOD with perimag compared to LS-008 is expected. Despite the lower signal, perimag is intensively used in the MPI community, and it is commercially available while LS-008 is not anymore. For an MPI scan using perimag, we have, to the authors' knowledge, measured and reconstructed the lowest reported iron content with our LOD of 8.5 ng.

Concerning the spatial resolution, we achieved an improvement from a resolution of ~5mm with the TxRx coil to ~3mm with the Rx_{mouse} coil. The same phantom was used in [31] to evaluate the performance of a passive receive coil insert, the passive dual-coil resonator (pDCR), that amplifies receive signals in a small frequency band around its tunable resonance frequency. In that work, for comparison also the TxRx coil and the Rx_{rat} coil were used, showing a spatial resolution of 3.5 mm for the TxRx and 2.5 mm for the Rx_{rat} coil. However, different particles and a higher DF amplitude were used than in this work; thus, only the performance increase can be compared rather than the total spatial resolution. Looking back to the iron LOD improvement from TxRx to Rx_{mouse} coil of a factor 10 and TxRx to Rx_{rat} of a factor 6.7 (Table I), the performance increase in spatial resolution behaves similar and shows the superior quality of the Rx_{mouse} coil.

B. Design Improvements

Using a gradiometric approach for either send or receive coil in an MPI system is very common (see [4], [17], [19], [20], [22], [51]). These gradiometers can feature one or more cancellation coil parts, where a symmetric setup around the pickup coil part is preferable for imaging. The common goal is the cancellation of the direct feedthrough of the excitation signal into the receive path, whereby the particle signal should not be attenuated. However, the cancellation coil parts are usually placed close to the pickup coil part due to geometric constraints. This either results in steeply declining sensitivity profiles and "zeros," if the cancellation coil parts are placed next to the pickup coil part, or part of the particle signal is directly canceled out if the cancellation coil parts are placed on top of the pickup coil parts for increased homogeneity. The presented Rx_{mouse} coil features cancellation coil parts with a larger radius, a radial gradiometer design, and placed next to the pickup coil part, thus eliminating the zeros and achieving an overall higher homogeneity compared to standard gradiometers [see Fig. 4(e)].

Positioning is another practical issue of gradiometric coils, as an imprecise placement of coil parts relative to each other leads to reduced feedthrough attenuation. Moreover, small tilts of coil parts can lead to unwanted crosstalk, especially with orthogonal excitation fields. Finally, axial and radial offsets between excitation and receive fields can result in shifted or skewed sensitivity profiles. With the Rx_{mouse} coil's optimized wiring, the mechanical scaffold, and axial and radial fixation mechanisms, precise and reproducible positioning is ensured. The symmetry of the Rx_{mouse} coil sensitivity can be observed in the spatial NA measurements [Fig. 4(c) and (d)] and the system matrix (Fig. 6).

C. Limitations

The effect of the gradiometer and the optimally tuned receive path is most prominent in the background measurements and the SNR spectra, especially observing the harmonics of the x-excitation field that are created by nonlinearities in the transmission chain. However, even a perfectly matched gradiometer will not cancel out all unwanted signal contributions, as its behavior is frequency-dependent, and thus, capacitive coupling between the involved coils causes small phase shifts in the receive signals preventing full attenuation [52]. Furthermore, for decreasing iron concentrations, only the lowest harmonics of the particle signal remain, which are attenuated by the BSF regardless of which receive coil is used. The LOD, as determined by the dilution series, is, thus, mostly influenced by the Rx_{mouse} coil's diameter. For measurements of iron contents higher than the LOD, the SNR gain due to the optimized receive chain including the gradiometric design enables to use higher frequency components in the reconstruction, which is directly correlated with improved spatial resolution [46] as validated in the spatial resolution experiment (Fig. 9).

Concerning limitations of this study, for the dilution series, we only measured the samples at specific regions within the FOV. However, the system matrices are essentially measurements of a particle sample at every position within the FOV and as shown in Fig. 6, their spatial patterns vary smoothly and the difference between TxRx and Rx_{mouse} coil is also consistent with the NA measurements along x- and y-axes (see Figs. 4 and 6). Thus, no degradation in imaging performance at other than the tested positions in the FOV can be expected.

Furthermore, we did not perform any tests regarding the long-term stability of the presented Rx_{mouse} coil. As the used materials are not expected to show significant signs of aging, no degradation in coil performance is anticipated. Temperature stability of the coil can be tracked using the built-in Pt100 sensor and shows approximately 3.5-K heating during the system matrix acquisitions. This temperature variation might cause slight changes in the receive signal, which are accounted for in the background correction both during the system matrix acquisition as well as during imaging experiments.

Lastly, all image reconstructions are highly influenced by the used reconstruction algorithm. We used the Kaczmarz algorithm, which is a very common algorithm for system matrix-based reconstruction in the MPI community. Due to the use of the system matrix-based approach, the choice of the reconstruction algorithm is independent of the used receive coil. Other algorithms that could enhance the reconstruction results include the nonnegative fused lasso method [53], the alternating direction method of multipliers (ADMM) [54], or even machine-learning-based methods such as the deep image prior [55] or the deep equilibrium model DEQ-MPI [56].

D. Future Work

There are several directions to explore to further optimize the coil design. One option is to add a frequency-dependent behavior to the cancellation coil parts such that they cancel out the excitation frequency but amplify the signal at higher harmonics. Preliminary simulations show that this could provide a further sensitivity improvement by 10%–20%. A resonant circuit is also utilized in the pDCR approach [31], which has so far been used as an insert for the TxRx coil to amplify high-frequency components for improved spatial resolution. This approach could also be used to amplify lower frequency components or be extended to enable multiple resonant frequencies for improved sensitivity and spatial resolution.

The superior performance of the Rx_{mouse} coil will be beneficial in many applications of MPI. Specifically, it can enable new cell tracking or drug delivery studies due to its high iron detection sensitivity. Furthermore, there is increasing interest in using MPI for supervision in hyperthermia treatments, which requires both good sensitivity and spatial resolution but also the ability to detect changes in particle signal due to variation in temperature and viscosity. The possibilities and limitations of MPI for this task can be evaluated using the Rx_{mouse} coil. Lastly, future applications of MPI also in clinical settings highly depend on available and tailored tracers. With the Rx_{mouse} coil, tracer performance can be evaluated with high precision in real imaging experiments, in contrast to the mere magnetic characterization in a magnetic particle spectroscopy system. Thereby, the coil can also be used to validate particle simulation models, which can then, in turn, be used to find optimized particle parameters for specific applications.

V. CONCLUSION

This article presents an evaluation of a dedicated mouse-sized Rx coil for the Bruker preclinical MPI scanner. Based on measurements with an NA, a sensitivity improvement from TxRx to Rx_{mouse} coil of 20–21 dB is realized in the MPI relevant frequency range from 10^2 to 10^3 kHz. Simulations and measurements of the sensitivity profile within the Rx_{mouse} coil show a decrease in sensitivity of only 9% within the DF FOV, proving the increased homogeneity of radial gradiometric receive coils compared to standard gradiometers. Due to the gradiometric design of the Rx_{mouse} coil, the background level decreases, leading to a gain in particle SNR of up to 86 dB and a nearly constant gain of 20 dB between 200 and 300 kHz. While a sensitivity improvement at lower frequencies translates to a higher iron detection efficiency, an increase in sensitivity for higher frequencies is important for a higher spatially resolved image reconstruction. The Rx_{mouse} coil achieves an iron LOD of 8.5 ng through an experimental dilution series, which is, to the authors' knowledge, the lowest reported LOD with perimag particles. With the TxRx coil, an LOD of 85 ng is achieved, which is a factor of 10 higher than the LOD determined with the Rx_{mouse} coil. For both coils, a linear relationship between reconstructed image intensities and iron mass is validated. Improved spatial resolution with the Rx_{mouse} coil was shown with a V-shaped resolution phantom.

In the future, the presented Rx_{mouse} coil will aid in many preclinical applications, and the presented technical improvements allow further advancement in the field of MPI. The higher sensitivity of the Rx_{mouse} coil is beneficial in various applications that directly benefit from the increased iron LOD, like cell tracking. Alternatively, the sensitivity can be traded off for higher spatially or temporally resolved MPI measurements, for applications like (cardio)vascular imaging.

REFERENCES

[1] B. Gleich and J. Weizenecker, "Tomographic imaging using the nonlinear response of magnetic particles," *Nature*, vol. 435, no. 7046, pp. 1214–1217, Jun. 2005.

[2] J. Franke et al., "Hybrid MPI-MRI system for dual-modal in situ cardiovascular assessments of real-time 3D blood flow quantification—A pre-clinical in vivo feasibility investigation," *IEEE Trans. Med. Imag.*, vol. 39, no. 12, pp. 4335–4345, Dec. 2020.

[3] P. Ludewig et al., "Magnetic particle imaging for assessment of cerebral perfusion and ischemia," *WIREs Nanomed. Nanobiotechnol.*, vol. 14, no. 1, p. e1757, Jan. 2022.

[4] P. Vogel et al., "IMPI: Portable human-sized magnetic particle imaging scanner for real-time endovascular interventions," *Sci. Rep.*, vol. 13, no. 1, p. 10472, Jun. 2023.

[5] O. Kosch, A. F. Sanches, Y. Özpeynirci, T. Liebig, and F. Wiekhorst, "Milisecond magnetic particle imaging of a 3D printed patient-specific cerebral aneurysm phantom with flow diverter stent," *Trans. AMMM*, vol. 5, no. S1, p. 808, 2023.

[6] H. Arami et al., "Tomographic magnetic particleimaging of cancer targeted nanoparticles," *Nanoscale*, vol. 9, no. 47, pp. 18723–18730, 2017.

[7] E. Y. Yu et al., "Magnetic particle imaging: A novel in vivo imaging platform for cancer detection," *Nano Lett.*, vol. 17, no. 3, pp. 1648–1654, Mar. 2017.

[8] E. E. Mason et al., "Concept for using magnetic particle imaging for intraoperative margin analysis in breast-conserving surgery," *Sci. Rep.*, vol. 11, no. 1, p. 13456, Jun. 2021.

[9] B. Zheng et al., "Quantitative magnetic particle imaging monitors the transplantation, biodistribution, and clearance of stem cells in vivo," *Theranostics*, vol. 6, no. 3, pp. 291–301, 2016.

[10] O. C. Sehl, A. V. Makela, A. M. Hamilton, and P. J. Foster, "Trimodal cell tracking in vivo: Combining iron- and fluorine-based magnetic resonance imaging with magnetic particle imaging to monitor the delivery of mesenchymal stem cells and the ensuing inflammation," *Tomography*, vol. 5, no. 4, pp. 367–376, Dec. 2019.

[11] H. Paysen et al., "Cellular uptake of magnetic nanoparticles imaged and quantified by magnetic particle imaging," *Sci. Rep.*, vol. 10, no. 1, p. 1922, Feb. 2020.

[12] A. V. Makela, M. A. Schott, O. C. Sehl, J. J. Gevaert, P. J. Foster, and C. H. Contag, "Tracking the fates of iron-labeled tumor cells in vivo using magnetic particle imaging," *Nanosc. Adv.*, vol. 4, no. 17, pp. 3617–3623, 2022.

[13] A. Remmo, O. Kosch, L. Kampen, A. Ludwig, F. Wiekhorst, and N. Löwa, "Counting cells in motion by quantitative real-time magnetic particle imaging," *Sci. Rep.*, vol. 14, no. 1, p. 4253, Feb. 2024.

[14] P. W. Goodwill, J. J. Konkle, B. Zheng, E. U. Saritas, and S. M. Conolly, "Projection X-space magnetic particle imaging," *IEEE Trans. Med. Imag.*, vol. 31, no. 5, pp. 1076–1085, May 2012.

[15] M. Graeser, T. Knopp, M. Grüttner, T. F. Sattel, and T. M. Buzug, "Analog receive signal processing for magnetic particle imaging," *Med. Phys.*, vol. 40, no. 4, Apr. 2013, Art. no. 042303.

[16] V. Schulz, M. Straub, M. Mahlke, S. Hubertus, T. Lammers, and F. Kiessling, "A field cancellation signal extraction method for magnetic particle imaging," *IEEE Trans. Magn.*, vol. 51, no. 2, pp. 1–4, Feb. 2015.

[17] M. Graeser et al., "Towards picogram detection of superparamagnetic iron-oxide particles using a gradiometric receive coil," *Sci. Rep.*, vol. 7, no. 1, pp. 1–13, Jul. 2017.

[18] H. Paysen et al., "Improved sensitivity and limit-of-detection using a receive-only coil in magnetic particle imaging," *Phys. Med. Biol.*, vol. 63, no. 13, Jul. 2018, Art. no. 13NT02.

[19] M. Irfan, N. Dogan, O. M. Dogan, and A. Bingolbali, "Development of magnetic particle imaging (MPI) scanner for phantom imaging of tracer agents," *IEEE Trans. Magn.*, vol. 58, no. 8, pp. 1–6, Aug. 2022.

[20] L. Yin et al., "A streamlined 3-D magnetic particle imaging system with a two-stage excitation feed-through compensation strategy," *IEEE Trans. Instrum. Meas.*, vol. 72, pp. 1–10, 2023.

[21] P. Vogel et al., "Dynamic linear gradient array for traveling wave magnetic particle imaging," *IEEE Trans. Magn.*, vol. 54, no. 2, pp. 1–9, Feb. 2018.

[22] K. Murase, S. Hiratsuka, R. Song, and Y. Takeuchi, "Development of a system for magnetic particle imaging using neodymium magnets and gradiometer," *Jpn. J. Appl. Phys.*, vol. 53, no. 6, Jun. 2014, Art. no. 067001.

[23] K. Murase, "Simultaneous correction of sensitivity and spatial resolution in projection-based magnetic particle imaging," *Med. Phys.*, vol. 47, no. 4, pp. 1845–1859, Apr. 2020.

[24] C. McDonough, J. Chrisekos, and A. Tonyushkin, "Tomographic magnetic particle imaging with a single-sided field-free line scanner," *IEEE Trans. Biomed. Eng.*, vol. 71, no. 12, pp. 3470–3481, Dec. 2024.

[25] Q. Wang et al., "Single-sided magnetic particle imaging device with offset field based spatial encoding," *IEEE Trans. Med. Imag.*, vol. 44, no. 4, pp. 1878–1889, Apr. 2025.

[26] E. Mattingly et al., "Design, construction and validation of a magnetic particle imaging (MPI) system for human brain imaging," *Phys. Med. Biol.*, vol. 70, no. 1, Jan. 2025, Art. no. 015019.

[27] F. Thieben et al., "System characterization of a human-sized 3D real-time magnetic particle imaging scanner for cerebral applications," *Commun. Eng.*, vol. 3, no. 1, p. 47, Mar. 2024.

[28] D. Eberbeck, C. L. Dennis, N. F. Huls, K. L. Krycka, C. Gruttner, and F. Westphal, "Multicore magnetic nanoparticles for magnetic particle imaging," *IEEE Trans. Magn.*, vol. 49, no. 1, pp. 269–274, Jan. 2013.

[29] J. Rahmer, J. Weizenecker, B. Gleich, and J. Borgert, "Signal encoding in magnetic particle imaging: Properties of the system function," *BMC Med. Imag.*, vol. 9, no. 1, pp. 1–21, Dec. 2009.

[30] E. U. Saritas, P. W. Goodwill, G. Z. Zhang, and S. M. Conolly, "Magnetostimulation limits in magnetic particle imaging," *IEEE Trans. Med. Imag.*, vol. 32, no. 9, pp. 1600–1610, Sep. 2013.

[31] D. Pantke et al., "Frequency-selective signal enhancement by a passive dual coil resonator for magnetic particle imaging," *Phys. Med. Biol.*, vol. 67, no. 11, Jun. 2022, Art. no. 115004.

[32] F. Thieben, T. Knopp, M. Boberg, F. Foerger, M. Graeser, and M. Möddel, "On the receive path calibration of magnetic particle imaging systems," *IEEE Trans. Instrum. Meas.*, vol. 72, pp. 1–15, 2023.

[33] P. Vogel, M. A. Rückert, T. Kampf, and V. C. Behr, "Highly flexible and modular simulation framework for magnetic particle imaging," 2022, *arXiv:2208.13835*.

[34] D. Pantke, F. Mueller, S. Reinartz, F. Kiessling, and V. Schulz, "Flow velocity quantification by exploiting the principles of the Doppler effect and magnetic particle imaging," *Sci. Rep.*, vol. 11, no. 1, p. 4529, Feb. 2021.

[35] P. Vogel et al., "Superspeed bolus visualization for vascular magnetic particle imaging," *IEEE Trans. Med. Imag.*, vol. 39, no. 6, pp. 2133–2139, Jun. 2020.

[36] A. Antonelli et al., "Development of long circulating magnetic particle imaging tracers: Use of novel magnetic nanoparticles and entrapment into human erythrocytes," *Nanomedicine*, vol. 15, no. 8, pp. 739–753, Apr. 2020.

[37] J. Wells, H. Paysen, O. Kosch, L. Trahms, and F. Wiekhorst, "Temperature dependence in magnetic particle imaging," *AIP Adv.*, vol. 8, no. 5, May 2018, Art. no. 056703.

[38] M. Utkur and E. U. Saritas, "Simultaneous temperature and viscosity estimation capability via magnetic nanoparticle relaxation," *Med. Phys.*, vol. 49, no. 4, pp. 2590–2601, Apr. 2022.

[39] A. Topcu, A. Alpman, M. Utkur, and E. U. Saritas, "Boosting viscosity sensitivity of magnetic particle imaging using selection field gradients," *Appl. Phys. Lett.*, vol. 125, no. 24, Dec. 2024, Art. no. 242405.

[40] S. Lei, J. He, X. Huang, H. Hui, Y. An, and J. Tian, "A novel local magnetic fluid hyperthermia based on high gradient field guided by magnetic particle imaging," *IEEE Trans. Biomed. Eng.*, vol. 71, no. 8, pp. 2528–2536, Aug. 2024.

[41] O. Buchholz et al., "In situ theranostic platform combining highly localized magnetic fluid hyperthermia, magnetic particle imaging, and thermometry in 3D," *Theranostics*, vol. 14, no. 1, pp. 324–340, 2024.

[42] A. Weber, F. Werner, J. Weizenecker, T. M. Buzug, and T. Knopp, "Artifact free reconstruction with the system matrix approach by overscanning the field-free-point trajectory in magnetic particle imaging," *Phys. Med. Biol.*, vol. 61, no. 2, pp. 475–487, Jan. 2016.

[43] T. Kluth and B. Jin, "Enhanced reconstruction in magnetic particle imaging by whitening and randomized SVD approximation," *Phys. Med. Biol.*, vol. 64, no. 12, Jun. 2019, Art. no. 125026.

[44] A. Dax, "On row relaxation methods for large constrained least squares problems," *SIAM J. Scientific Comput.*, vol. 14, no. 3, pp. 570–584, May 1993.

[45] J. Weizenecker, J. Borgert, and B. Gleich, "A simulation study on the resolution and sensitivity of magnetic particle imaging," *Phys. Med. Biol.*, vol. 52, no. 21, pp. 6363–6374, Nov. 2007.

[46] J. Rahmer, J. Weizenecker, B. Gleich, and J. Borgert, "Analysis of a 3-D system function measured for magnetic particle imaging," *IEEE Trans. Med. Imag.*, vol. 31, no. 6, pp. 1289–1299, Jun. 2012.

[47] U. Heinen, A. Weber, J. Franke, H. Lehr, and O. Kosch, "A versatile MPI system function viewer," *IJMPI*, vol. 3, no. 2, Jun. 2017, Art. no. 1706006.

[48] L. Wöckel et al., "Long-term stable measurement phantoms for magnetic particle imaging," *J. Magn. Magn. Mater.*, vol. 471, pp. 1–7, Feb. 2019.

[49] F. Mohn et al., "Characterization of the clinically approved MRI tracer resotran for magnetic particle imaging in a comparison study," *Phys. Med. Biol.*, vol. 69, no. 13, Jul. 2024, Art. no. 135014.

[50] R. M. Ferguson et al., "Magnetic particle imaging with tailored iron oxide nanoparticle tracers," *IEEE Trans. Med. Imag.*, vol. 34, no. 5, pp. 1077–1084, May 2015.

[51] D. Pantke, N. Holle, A. Mogarkar, M. Straub, and V. Schulz, "Multifrequency magnetic particle imaging enabled by a combined passive and active drive field feed-through compensation approach," *Med. Phys.*, vol. 46, no. 9, pp. 4077–4086, Sep. 2019.

[52] H. Radermacher, F. Schrank, D. Pantke, F. Mueller, and V. Schulz, "Automated tuning coil loading for improved passive compensation for multi-frequency MPI," in *Proc. EMIM*, Porto, Portugal, Mar. 2024, pp. 1–18. [Online]. Available: https://www.eventclass.it/emim2024/scientific/online-program/session?s=PS+09\#e165

[53] M. Storath et al., "Edge preserving and noise reducing reconstruction for magnetic particle imaging," *IEEE Trans. Med. Imag.*, vol. 36, no. 1, pp. 74–85, Jan. 2017.

[54] S. İlbey, C. B. Top, A. Güngör, T. Çukur, E. Ü. Sarıtaş, and H. E. Güven, "Comparison of system-matrix-based and projection-based reconstructions for field free line magnetic particle imaging," *Int. J. Magn. Part. Imag.*, vol. 3, no. 1, pp. 1–8, Mar. 2017.

[55] S. Dittmer, T. Kluth, D. O. Baguer, and P. Maass, "A deep prior approach to magnetic particle imaging," in *Machine Learning for Medical Image Reconstruction*, F. Deeba, P. Johnson, T. Würfl, and J. C. Ye, Eds., Cham, Switzerland: Springer, 2020, pp. 113–122.

[56] A. Güngör, B. Askin, D. A. Soydan, C. B. Top, E. U. Saritas, and T. Çukur, "DEQ-MPI: A deep equilibrium reconstruction with learned consistency for magnetic particle imaging," *IEEE Trans. Med. Imag.*, vol. 43, no. 1, pp. 321–334, Jan. 2024, doi: 10.1109/TMI.2023.3300704.

Franziska Schrank received the B.Sc. and M.Sc. degrees in physics from RWTH Aachen University, Aachen, Germany, in 2019 and 2020, respectively, where she is currently pursuing the Ph.D. degree with the Chair of Imaging and Computer Vision and the Institute for Experimental Molecular Imaging, under the supervision of Volkmar Schulz.

Her research interests include signal and image processing and reconstruction in magnetic particle imaging, and machine learning.

Harald Radermacher, photograph and biography not available at the time of publication.

Jochen Franke received the Diploma degree in engineering physics from the University of Applied Sciences Münster, Münster, Germany, in 2008, and the M.Sc. degree in biomedical engineering and the Ph.D. degree in theoretical medicine from RWTH Aachen University, Aachen, Germany, in 2010 and 2024, under the supervision of Volkmar Schulz.

Since 2012, he has been an Employee at Bruker BioSpin GmbH and Company KG, Ettlingen, Germany, first as a Research Program Manager, then as a Product Manager and later a Research and Development Program Manager, and finally, Group Leader of magnetic particle imaging since 2024.

Sébastien Breham, photograph and biography not available at the time of publication.

Fabian Kiessling received the Dr.Med. degree from Heidelberg University, Heidelberg, Germany, in 2001.

Until 2008, he worked at the Departments of Radiology and Medical Physics in Radiology, German Cancer Research Center, Heidelberg, and received the board certification as a Radiologist. Since 2008, he has been leading the Institute for Experimental Molecular Imaging, RWTH Aachen University, Aachen, Germany. He authored over 500 publications and book chapters, and edited four books.

Dr. Kiessling is a fellow of WMIS. He was the Program Chair of WMIC in 2016 and served as the President of European Society for Molecular Imaging. Since 2019, he has been on the list of Clarivate's Highly Cited Researchers.

Volkmar Schulz (Senior Member, IEEE) received the Dipl.-Ing. (Fh) degree in electrical engineering from Bielefeld University of Applied Sciences, Bielefeld, Germany, in 1993, the Dipl.-Ing. degree in information technology, and the Dr.-Ing. degree in electrical engineering from the University of Paderborn, Paderborn, Germany, in 1996 and 2001, respectively.

From 2000 to 2005, he worked at Philips Research, Hamburg, Germany, where he developed MRI systems before focusing on hybrid PET/MRI technologies. In 2013, he was appointed as a Full Professor of physics of molecular imaging systems at RWTH Aachen University, Aachen, Germany, and became the Head of the Chair of Imaging and Computer Vision in 2024. He is the Co-Founder and the CEO/CTO of the Hyperion Hybrid Imaging Systems, Aachen, established in 2019. He holds over 70 patent applications in medical imaging.

Dr. Schulz received the Fraunhofer Attract Prize in 2023. He served on the IEEE Nuclear Medicine Imaging Steering Committee. He regularly contributes to international conferences and editorial boards in the field.